Nuclear Science and Techniques (2026) 37:62
https://doi.org/10.1007/s41365-025-01881-3

The measurement of the energy correlations between two ^{252}Cf prompt fission neutrons

Huai-Yong Bai[1] · **Hang Li**[1] · **Hong-Jun Zhang**[1] · **Cheng-Guo Pang**[1] · **Ming Su**[1] · **Zhong-Hua Xiong**[1] · **Ji Wen**[1] · **Fan Gao**[1] · **Chen-Guang Li**[1] · **Xiao-Dong Wang**[1] · **Li-Sheng Yang**[1]

Received: 10 June 2025 / Revised: 14 October 2025 / Accepted: 21 November 2025 /

Abstract

The energy correlations of prompt fission neutrons have not yet been considered in the related coincidence and multiplication measurement techniques. To measure and verify the energy correlations, an experiment was performed with a total measurement duration of approximately 1200 h. In the experiment, eight CLYC detectors and sixteen EJ309 liquid scintillation detectors were utilized, and the fission moment was tagged with the measured fission γ-rays. The relative ratios of the energy spectra of the neutrons correlated with different energy neutrons to the ^{252}Cf fission neutron energy spectra were obtained. The present results may be helpful for studying fission physics and nuclear technology applications.

Keywords Energy correlations · Prompt fission neutrons · Energy spectrum · Fission γ-rays

1 Introduction

Neutron coincidence and multiplication measurement techniques have been developed as nondestructive assay methods for special nuclear materials and nuclear fuels over the past few decades [1–5]. The related physical foundation is that more than one prompt fission neutron may be emitted from a spontaneous or induced fission event, resulting in the detection of time-correlated neutron events. In addition to the time correlation, the neutron energies emitted in one fission event are interdependent. On the one hand, the neutron energy distributions depend on the actual number of emitted neutrons [6]. However, the energies of the neutrons are affected by the direction and velocity of the corresponding fission fragments, as most of the prompt fission neutrons are emitted from the fast moving fission fragments. Therefore, the energies of the neutrons emitted from the same fission fragment or different fission fragments moving in opposite directions are connected [7]. However, owing to the lack of available energy correlation data, the energy correlations of prompt fission neutrons have not been considered in neutron coincidence and multiplication measurement techniques, despite their wide application and use in some measurement fields as standard methods [8]. This may lead to some measurement deviations, as the detection efficiency is affected by the neutron energy, particularly for fast neutron coincidence and multiplication measurement techniques.

To date, several codes capable of simulating correlations among emitted neutrons in fission reactions on an event-by-event basis have been developed, such as MCNPX-POLIMI, CGMF, and FREYA [9–13]. However, these codes require reliable experimental data to validate their models [14, 15]. In 2019, P. F. Schuster et al. measured the prompt fission neutron energy correlation of ^{252}Cf for the first and only time. In the experiment, the Chi-Nu detector array, consisting of 54 EJ309 liquid scintillation detectors with a diameter of 17.78 cm and thickness of 5.08 cm, was used to detect the prompt fission neutrons, and a fission chamber with a ^{252}Cf source, whose fission rate was 2.98×10^5 s^{-1}, was used to measure the moment when the fission event occurred [14, 16]. According to their measurements, the correlations between the average energies of the paired neutrons with emission angles of 85° and 175° were negative and positive, respectively. However, as they claimed in their paper, the

---

This work was supported by the National Natural Science Foundation of China (No. 12105257) and the Research and Development Fund (No. JMJJ202401).

✉ Zhong-Hua Xiong
xiongzhonghua@caep.cn

[1] Institute of Materials, China Academy of Engineering Physics, Jiangyou 621907, China

result was inconclusive because the experimental uncertainties were noticeable, resulting in the calculated slopes being within 2σ of zero [14].

To obtain more detailed data on the energy correlations of ^{252}Cf prompt fission neutrons, we conducted an experimental study. Before the measurement, a Monte Carlo simulation was developed to predict the energy correlation and instruct the measurement, in which the neutron energies were obtained using the measured time-of-flight. In most existing measurements, the fission moment, that is, the start moment of the neutron flight, was tagged by detecting the fission fragment with a fission chamber [17, 18]. However, this tagging technique may not be suitable for measuring neutron energy correlations. In the fission chamber, the ^{252}Cf source is typically embedded on a metal foil or plate substrate. Most fission fragments would lose part of their energy before entering the sensitive region of the chamber, especially those fragments with large emission angles with respect to the normal of the metal foil or plate substrate. Therefore, the difference in the detection efficiencies of the fission fragments with different emission angles was noticeable. This may result in some measurement deviations because the prompt fission neutron energy correlations are associated with the corresponding fission fragment moving direction, as introduced above. For ^{252}Cf, approximately 11.6 γ-rays are emitted per spontaneous fission [19]. Because the time interval between the emission moments of almost all fission γ-rays with energies exceeding 0.3 MeV and their corresponding fission moment is less than 0.5 ns, and the flight speed of γ-ray is well known, the fission moment can be precisely determined by the detection moment of the fission γ-ray if the measurement threshold is set above 0.3 MeV [20]. This indicates that the fission moment can be accurately tagged using the fission γ-rays. Therefore, in the present experiment, the fission moment was tagged with fission γ-rays detected by scintillation detectors rather than fission fragments detected by a fission chamber.

The present manuscript presents the experimental study of the energy correlations between neutrons emitted at 90° and 180° relative to each other. In the measurement, the prompt fission neutrons were measured using sixteen small EJ309 liquid scintillation detectors (5.08 cm in diameter and 5.08 cm in thickness) because of their superior PSD performance, and the fission γ-rays were detected with eight CLYC detectors (2.54 cm in diameter and 2.54 cm in thickness) [21]. The measured neutron energy spectra, correlated with different energy neutrons, were presented ranging from 1 to 5 MeV for the first time and compared with those obtained using the Monte Carlo simulation.

2 Monte Carlo simulation

Because most prompt fission neutrons are evaporated from fully accelerated fission fragments, their energy and direction in the laboratory system are significantly affected by the energy and direction of the associated fission fragments. Therefore, the yields and energies of the fission fragments, as well as the number of neutrons evaporated from specific fission fragments, are required to predict the energy correlation. A flowchart of the developed Monte Carlo simulation is shown in Fig. 1. The fission events were simulated one by one, and the procedure was generally divided into three stages: first, the generation of the two fission fragments; second, the generation of the prompt fission neutrons; and finally, the statistics of the neutrons.

2.1 Generation of the two fission fragments

The mass of the light fission fragment M_{L} was randomly sampled with a probability proportional to the yields shown in Fig. 2 [22]. The mass of the paired heavy fission fragment M_{H} is $252u - M_{\mathrm{L}}$. Then, the total kinetic energy TKE and its corresponding uncertainty σ_{TKE} were determined using the total kinetic energy distribution and the corresponding uncertainty distribution as functions of the light fragment mass, as shown in Fig. 3. The specific total kinetic energy of the sampled fission fragment pair E_{T} was specified as $TKE + \Delta TKE$, where ΔTKE was randomly sampled from the normal distribution with a standard deviation of σ_{TKE}. The kinetic energy of the light fission fragment E_{L} was determined as:

$$E_{\mathrm{L}} = \frac{M_{\mathrm{H}} E_{\mathrm{T}}}{M_{\mathrm{L}} + M_{\mathrm{H}}}. \tag{1}$$

The kinetic energy of the heavy fission fragment E_{H} was equal to $E_{\mathrm{T}} - E_{\mathrm{L}}$. Finally, the direction of the light fission fragment in the laboratory system was sampled from an isotropic distribution, and the direction of the heavy fission fragment was opposite to that of the light fragment.

2.2 Generation of the prompt fission neutrons

The evaporation of the neutrons was simulated via a cascade process for the light fission fragments, followed by the heavy fission fragments. The number of neutrons emitted from fission fragments with different masses and the corresponding uncertainties are shown in Fig. 4 [22]. Because σ_{TKE} is known, σ_{ν} can be calculated. The number of neutrons N evaporated from the sampled light fission fragment was $\nu + \Delta\nu$, where $\Delta\nu$ was randomly sampled from the normal distribution with a standard deviation of σ_{ν}. In almost all

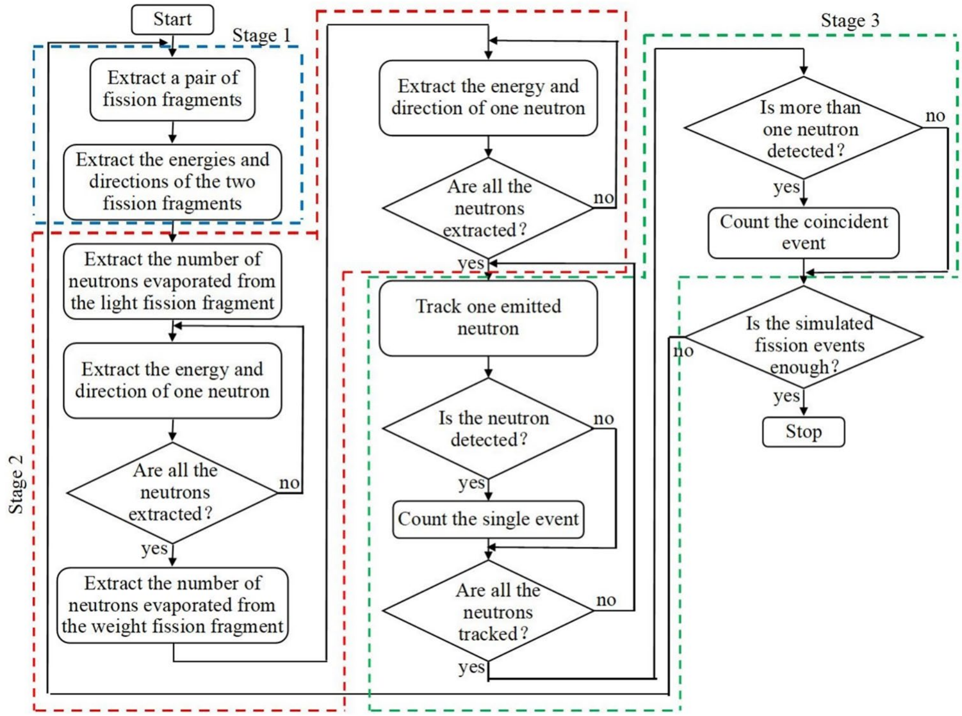

Fig. 1 The flowchart of the Monte Carlo simulation of the prompt fission neutron energy correlation

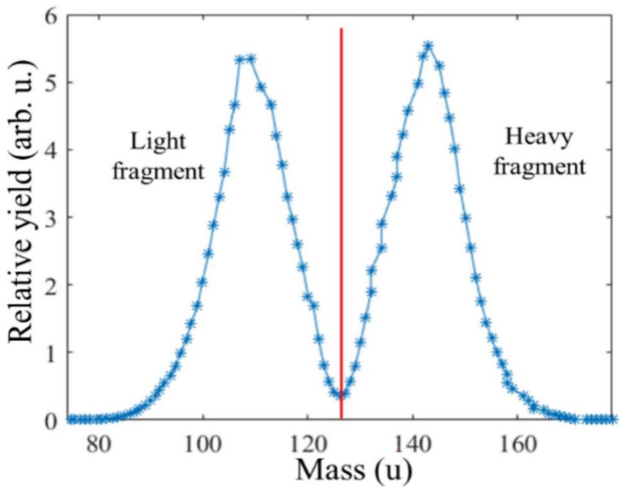

Fig. 2 The yields of the fission fragments with different masses [22]

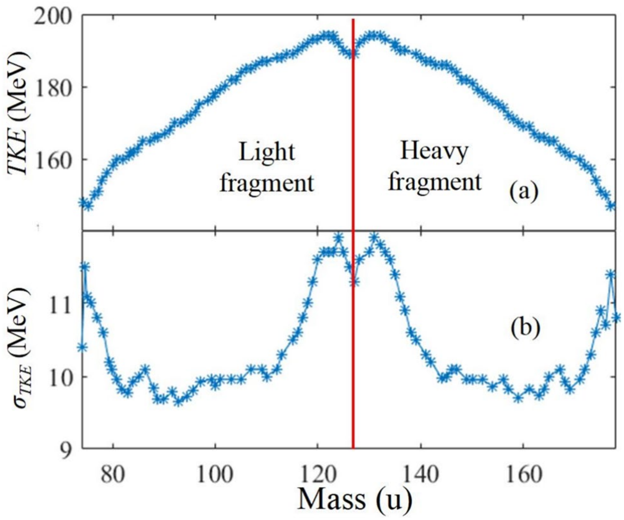

Fig. 3 The distributions of the total kinetic energy (**a**) and the corresponding uncertainty (**b**) versus the fragment mass [22]

cases, N was a non-integer. Thus, N was decomposed into an integer part I_N (the largest integer smaller than N) and a decimal part D_N (where $D_N = N - I_N$). Then, a random number e in [0, 1] was sampled and compared with D_N. If e was smaller than D_N, the actual number of neutrons R_N emitted from the light fission fragment was $I_N + 1$; otherwise R_N equaled I_N.

According to the standard nuclear evaporation theory, the fission neutron energy spectrum Φ in the center-of-mass system of the fission fragment can be described as [22]:

$$\Phi(E) \propto E^{\lambda} \exp(-E/T_{\text{eff}}) = E^{\lambda} \exp(-1.09E/T), \tag{2}$$

where λ is the cascade neutron emission coefficient and T denotes the temperature of the fission fragment, as shown in Fig. 5 [22]. According to the energy distribution calculated using Eq. (2), the energy of a neutron in the center-of-mass system was sampled. The direction of the neutron was sampled from an isotropic distribution. Thereafter, the energy and direction of the neutron in the laboratory

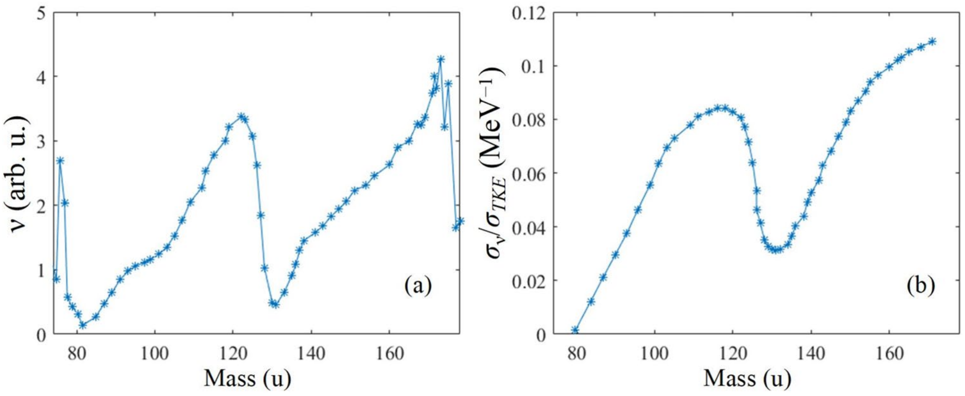

Fig. 4 The number (**a**) and the corresponding uncertainty (**b**) of the neutrons evaporated from fission fragments with different masses [22]

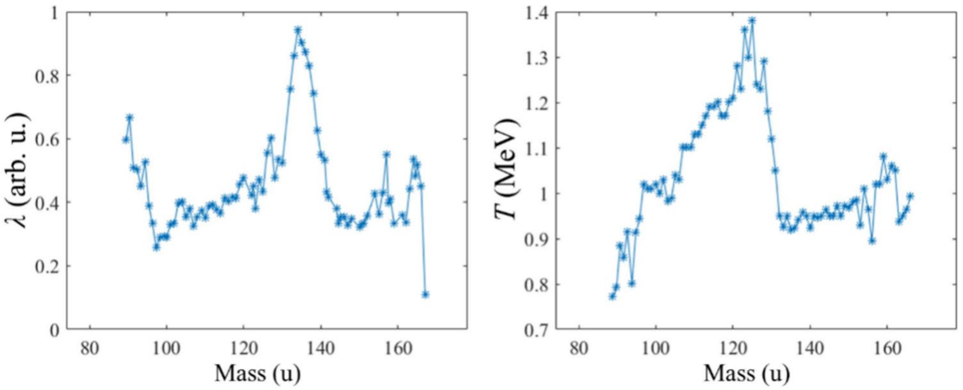

Fig. 5 The cascade neutron emission coefficients (**a**) and temperatures (**b**) versus the fragment masses [22]

system, together with those of the light fission fragments, were calculated under the constraints of energy and momentum conservation. The mass of the light fission fragment equals $M_{\mathrm{L}} - n$, where n represents the number of neutrons evaporated from the light fission fragment until this point. Finally, the energy and direction of the neutron were stored in a queue.

Neutrons were evaporated one by one using the same process until R_N neutrons have been evaporated from the light fission fragment. After the generation of neutrons evaporated from the light fission fragment, the neutrons evaporated from the heavy fission fragment were processed in a similar manner.

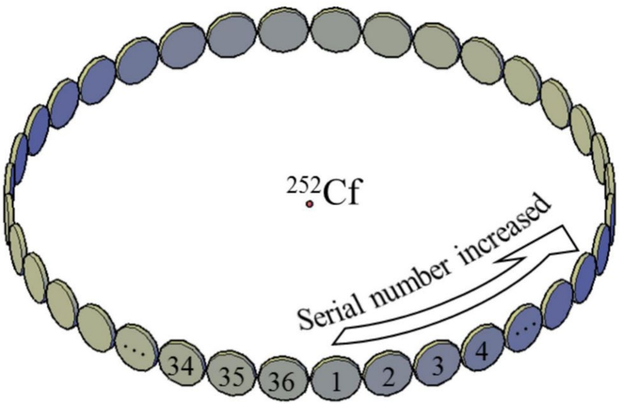

Fig. 6 (Color online) The layout of the detectors in the simulation

2.3 Statistics of the neutrons

After the generation of prompt fission neutrons, they were tracked to obtain their energy correlations. As shown in Fig. 6, 36 surface detectors (with a radius of 5 cm) were positioned on a circle (with a radius of 60 cm), and a ^{252}Cf source was located at the center of the circle. The angle between the adjacent surface detector normals was 10°. The fission events, stored in the queue with the energy and directional information of the emitted neutrons, were tracked individually. If a neutron reached any of the detectors, it was counted as a single event. As shown in Fig. 7, the simulated energy spectrum of the single events agrees well with the ^{252}Cf prompt fission neutron energy spectrum recommended by IAEA with the relative deviation smaller than 0.6% [23]. After all the neutrons were tracked, if multiple neutrons emitted in the same fission event reached the detectors, each two neutrons were paired as a group. In this process, the neutron reaching the detector with a smaller serial number was designated as the first one. In the present work,

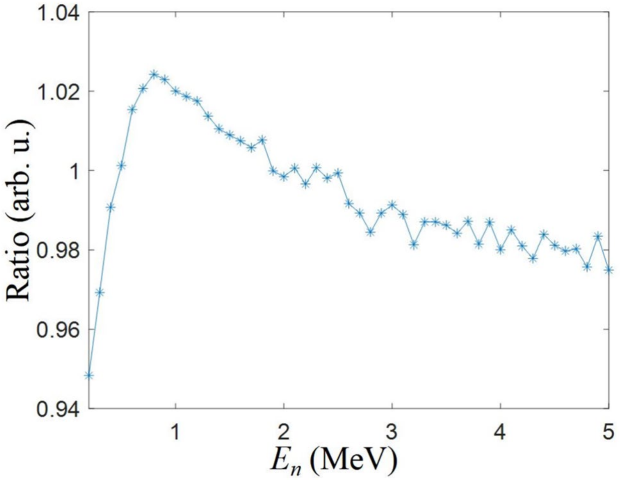

Fig. 7 The ratio of the simulated ^{252}Cf prompt fission neutron energy spectrum to that recommended by IAEA [23]

the correlation events at 0° to 180° with the interval of 30° (the angle between the two neutron directions) were counted.

As presented in Fig. 8, the distributions of the correlated events at 90° and 180° are noticeably different from each other. The neutron energies corresponding to the highest counts at 90° and 180° are 2.6 MeV and 3.0 MeV. To present the energy correlations more clearly, the counts at each angle were normalized in two steps, as shown in Fig. 9. First, the total counts in each column with neutron energies ranging from 1–5 MeV were normalized. Second, the count distributions in each column were normalized to the simulated ^{252}Cf prompt fission neutron energy spectrum. As Fig. 9 shows, the neutron energy correlations vary with angle. The second neutron energy trends toward lower values for the correlated events at near 90°, whereas it trends toward higher values for the correlated events at near 0° or 180°. These trends increased with the first neutron energy. Because the crosstalk effect in the measurement is non-negligible for the correlated events at angles smaller than 75° [14], the energy correlations at 90° and 180° are measured in the present work as representative cases.

In the measurement, a triple coincident measurement is required, resulting in a very low detection efficiency. According to the test, the time resolution of the measurement was approximately 1.5 ns. Therefore, the length-of-flight of neutrons was set to 62.5 cm to balance both neutron detection efficiency and energy resolution measured using the TOF (time-of-flight) technique.

3 Experiments

3.1 Experimental setup

The experimental setup is illustrated in Fig. 10. A ^{252}Cf source with a fission rate of approximately $1.3 \times 10^5\ \mathrm{s}^{-1}$ was used for the experiment. The source was sealed in a stainless steel capsule (~2 mm in diameter and ~5 mm in height) and suspended vertically at a height of 1.5 m above the floor using a fine nylon thread to minimize neutron scattering effects on the detection by the EJ309 liquid scintillation detectors. All detectors were mounted on aluminum supports. Every four EJ309 liquid scintillation detectors were combined into an array. The angle between the normals of the adjacent arrays was fixed at 90°. The distance from the ^{252}Cf source to the front faces of the eight CLYC detectors was 6±0.1 cm, and that to the front faces of the sixteen EJ309 liquid scintillation detectors was 60±0.1 cm. Since the thickness of the EJ309 liquid scintillation detector is 5.08 cm, the uncertainty of the neutron flight path length σ_{L} is 2.15 cm calculated as:

$$\sigma_{\mathrm{L}} = \sqrt{\int_{-0.5H}^{0.5H} \frac{x^2 \mathrm{d}x}{H} + \sigma_{\mathrm{p}}^2}, \tag{3}$$

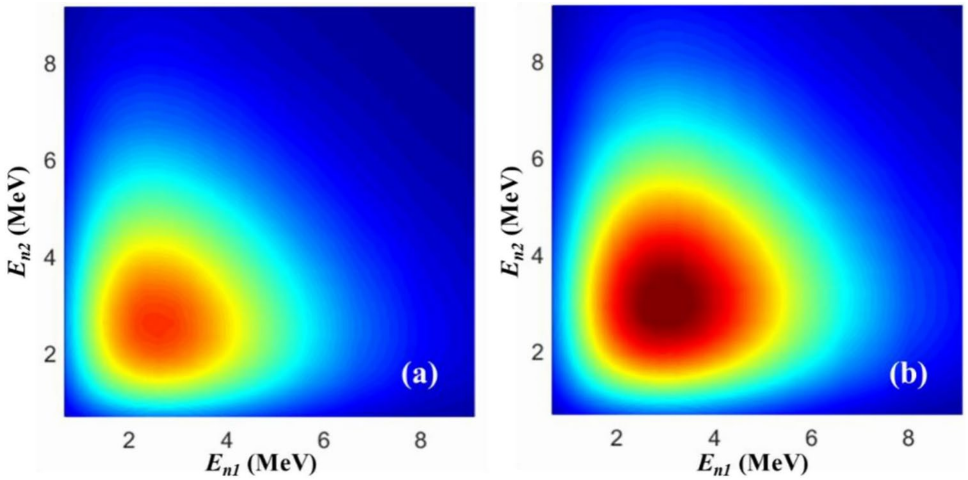

Fig. 8 (Color online) The simulated correlation events at 90° (**a**) and 180° (**b**)

Fig. 9 (Color online) The simulated neutron energy correlations at 0° (**a**), 30° (**b**), 60° (**c**), 90° (**d**), 120° (**e**), 150° (**f**) and 180° (**g**)

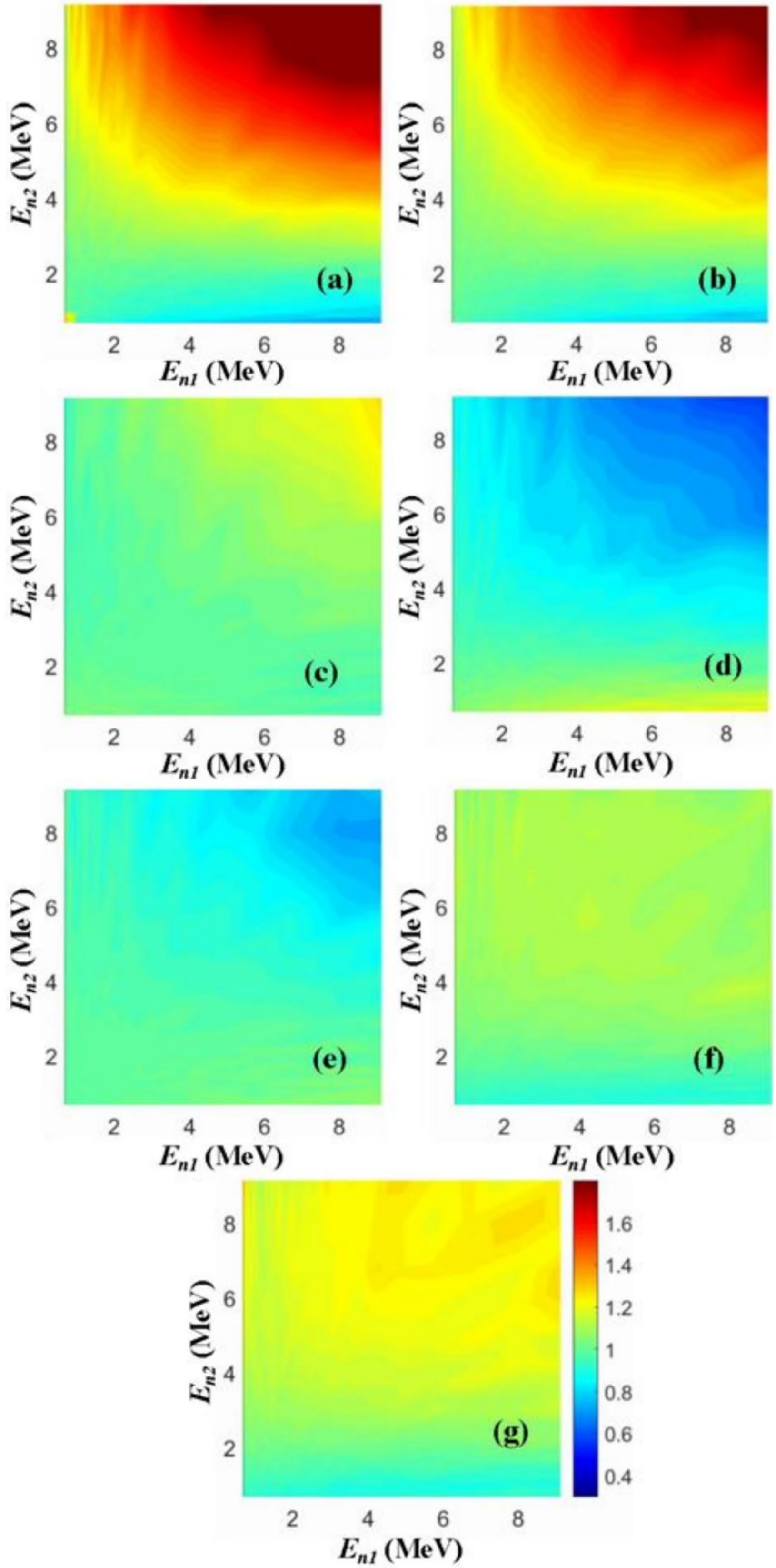

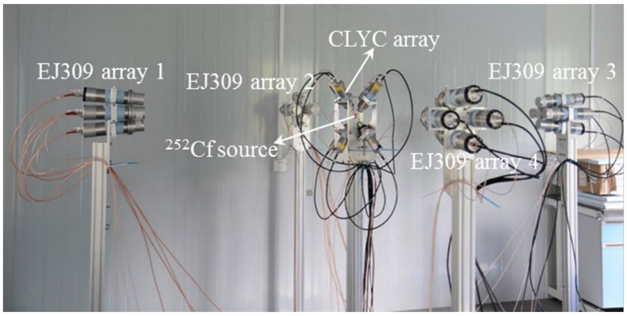

Fig. 10 (Color online) The experimental setup photograph

where H is the thickness of the EJ309 liquid scintillation detector, and σ_p represents the uncertainty in the distance from the ^{252}Cf source to the front faces of the EJ309 liquid scintillation detectors.

The detector signals were acquired using two CAEN VX1730B digitizers. Each digitizer has 16 input channels with a sampling frequency of 500 MS/s. One digitizer was connected to the eight CLYC detectors, and the other was connected to the sixteen EJ309 liquid scintillation detectors. Both digitizers were operated in list mode with the time-stamp (T), long and short gate integrated charges (Q_L and Q_S) of every event being saved for off-line analysis. The pulse height (PH) and pulse shape discrimination (PSD) parameter can be calculated as [24, 25]:

$$PH = C_A Q_L, \tag{4}$$

$$PSD = C_P \left(1 - \frac{Q_S}{Q_L}\right), \tag{5}$$

where C_A and C_P are calibration factors of PH and PSD, respectively.

3.2 Calibration of the detectors

Before the measurement, the eight CLYC detectors and the sixteen EJ309 liquid scintillation detectors were calibrated with ^{60}Co (1.33 and 1.17 MeV) and ^{22}Na (1.28 and 0.55 MeV) γ sources as shown in Fig. 11. The signal gains were almost equivalent for the eight CLYC detectors by adjusting their working high voltages. Similar adjustments to the working high voltage were also applied to the sixteen EJ309 liquid scintillation detectors. In the calibration of the eight CLYC detectors, both the photo peaks and Compton edges were used, and in that of the sixteen EJ309 liquid scintillation detectors, only the Compton edges were utilized. The method for determining the Compton edges was described in Ref. [26, 27]. The corresponding Compton electron energy E_e is

$$E_e = \frac{2E_\gamma^2}{m_0C^2 + 2E_\gamma}, \tag{6}$$

where E_γ denotes the γ-ray energy and m_0C^2 represents the electron rest mass energy (0.511 MeV).

In Fig. 11(a), the Compton edge corresponding to the Compton electron energy of 1.12 MeV was obscured because it overlapped with the tail of the 1.17 MeV photo peak. The position of the Compton edge corresponding to the Compton electron energy of 0.38 MeV could not be determined accurately because it was significantly affected by the measurement threshold. Consequently, these two Compton edges were not used in the calibration of the eight CLYC detectors.

3.3 Measurement

The experiment was conducted for a total measurement duration of approximately 1200 h. Because two VX1730B digitizers were used to acquire the detector signals in the experiment, they must be operated in a time-synchronized mode to obtain the accurate TOF data. To achieve this, the

Fig. 11 (Color online) The pulse height spectra induced by the ^{60}Co and ^{22}Na γ sources for a CLYC detector (**a**) and a EJ309 liquid scintillation detector (**b**)

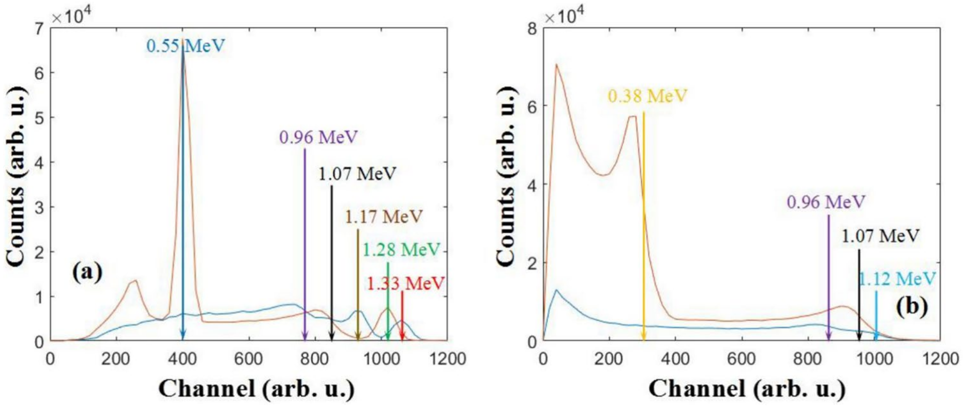

two digitizers shared the internal clock of the one connected to the eight CLYC detectors, and the synchronization settings were configured via the data acquisition software COMPASS, as described in the COMPASS User Manual [28]. According to our synchronization test with a pulse generator DT5810, the synchronization accuracy was better than 0.1 ns. Although this synchronization accuracy contributes to the experimental time resolution, its influence can be ignored because it is much smaller than the experimental time resolution of 1.5 ns.

4 Results and discussion

4.1 Data analysis

With the experimental data, the PH-PSD two dimensional spectra of the eight CLYC detectors and the sixteen EJ309 liquid scintillation detectors were obtained, as illustrated in Fig. 12. By applying optimal discrimination thresholds, event types (γ-rays or neutrons) can be identified.

In the present measurement, the measurement thresholds of the CLYC detectors were approximately 250 channels (0.3 MeV for γ-ray), and those of the EJ309 liquid scintillation detectors were approximately 50 channels (0.5 MeV for protons). Although the low measurement threshold for the EJ309 liquid scintillation detector could lead to the misidentification of event types using PSD for low pulse height events, the probability of classifying a γ-ray event as a neutron event was low because of the significant TOF difference between γ-ray and neutron events, as shown in Fig. 13.

Figure 13 illustrates the TOF distribution of single neutron events detected by the sixteen EJ309 liquid scintillation detectors. To suppress the interference of accidental coincidences, triple time correlation coincidence was adopted in the data analysis; that is, a neutron event was required to correlate with at least two γ-rays detected by either the CLYC or EJ309 liquid scintillation detectors. The start moment of TOF T_0 is

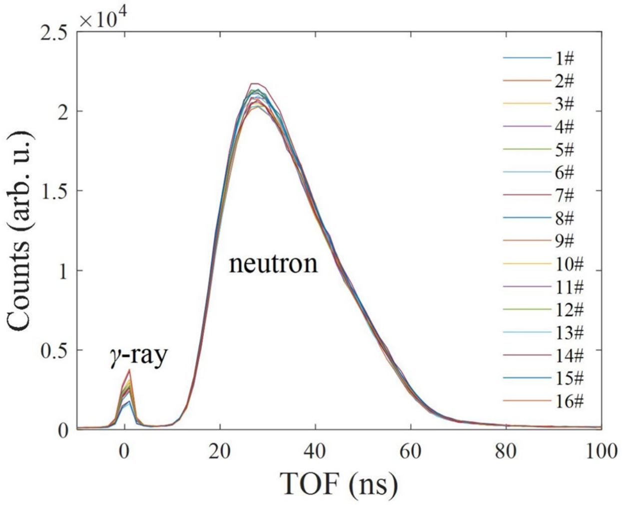

Fig. 13 (Color online) The TOF distribution for the “neutron events” decided by PSD

$$T_0 = \frac{\sum_k T_k PH_k}{\sum_k PH_k}, \tag{7}$$

where T_0 denotes the time-stamp, and the subscript k represents the serial number of the corresponding detected γ-rays. The coincident time window was −200 to 200 ns. The average count S_b in the time window from −200 to −50 ns was taken as the accidental coincident background. The net single neutron events S_{net} can be derived by subtracting S_b from the TOF distribution shown in Fig. 13. Theoretically, S_{net} was proportional to the detection efficiency ε and neutron flux ϕ as

$$S_{net,i} = \phi_i \varepsilon_i, \tag{8}$$

where the subscript i represents the serial number of the divided TOF bin.

The neutron coincident events at 90° and 180° are shown in Fig. 14. Triple time correlation coincidence was employed in the data analysis, that is, two neutrons and

Fig. 12 (Color online) The PH-PSD two dimensional spectra of a CLYC detector (**a**) and an EJ309 liquid scintillation detector (**b**)

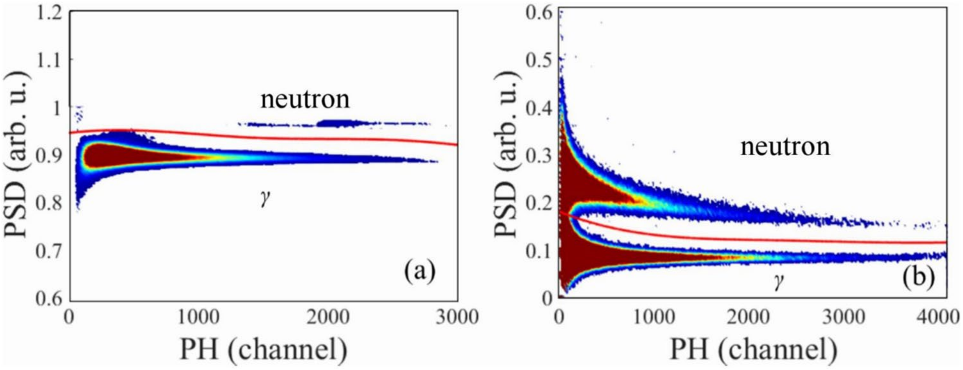

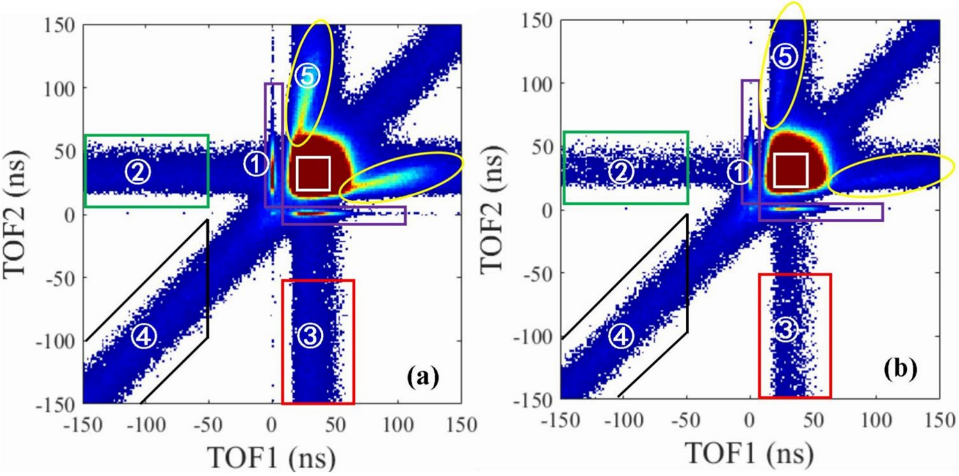

Fig. 14 (Color online) The neutron coincident events at 90° (**a**) and 180° (**b**)

at least one γ-ray were required to define one coincident event. There are five types of interferential events. The first is the γ-ray event shown in the purple box. These events do not noticeably affect the measurement of the neutron event shown in the white box because the TOF difference between γ-rays and neutrons is significant. The second one, shown in the green box, indicates that the first neutron is an accidental coincident neutron. The related interference can be deducted using the counts of each column in the white box to subtract the average counts of each column in the corresponding region with TOF ranging from −150 ns to −50 ns for the first neutron. The third one, shown in the red box, is that the second neutron is an accidental coincident neutron, and the related interference can be subtracted using a data analysis approach similar to that for the second one. The fourth one shown in the black frame is that the γ-ray is an accidental coincident γ-ray. The corresponding interference can be deducted using the following two steps. In the first step, the region with TOF ranging from −150 ns to −50 ns for the first neutron was scanned along the diagonal line using a scanning box identical to the white box shown in Fig. 14. During the scanning process, the average count of every bin in the scanning box was calculated. In the second step, the corresponding interference was deducted using the counts in the white box to subtract the average counts of the corresponding bins in the scanning box. The fifth one is the events induced by crosstalk, that is, the neutron detected by the second detector is the same one that is scattered and detected by the first detector. Although the accurate subtraction of this interference is difficult, it can be significantly mitigated by restricting the TOF to the range of 19–46 ns. This conclusion was drawn based on the Monte Carlo simulation performed by JMCT, as shown in Fig. 15 [29].

After the subtraction of the interference events mentioned above, the net neutron coincident events D can be obtained. To obtain the relative deviation between the neutron energy spectrum of ^{252}Cf prompt fission neutrons and that of the neutrons correlated with different energy neutrons, three calculation steps were executed. First, the net neutron coincident events D were compared with the net single neutron events S_{net} to obtain the relative ratio R as:

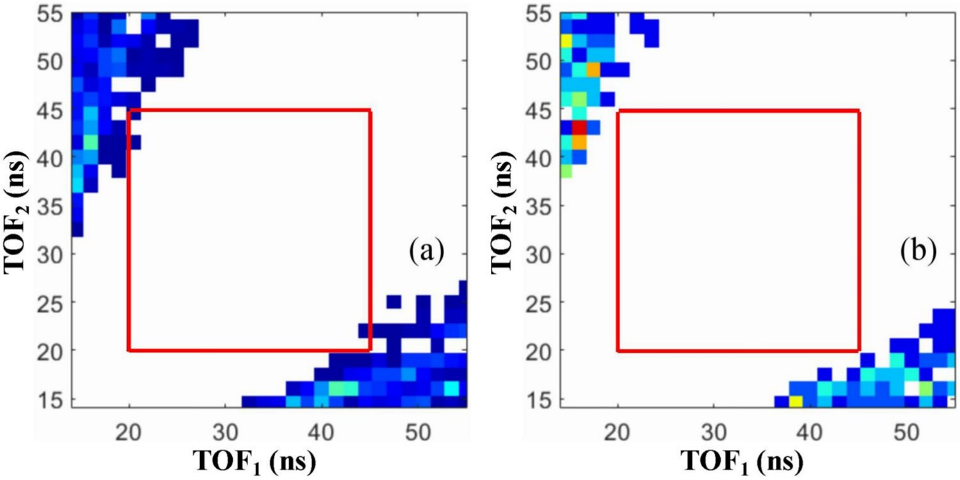

Fig. 15 (Color online) The simulated cross talk events at 90° (**a**) and 180° (**b**)

$$R_{i,j}=\frac{D_{i,j}}{S_{\mathrm{net},j}}, \tag{9}$$

where the subscripts i and j of R and D separately denote the TOF bin serials of the first and second detected neutrons, and the subscript j also represents the TOF bin serial of the net single events for S_{net}. It should be mentioned that the influence of the detection efficiencies for different energy neutrons is canceled out in this step. Second, the relative ratios R were normalized over the TOF_2 region ranging from 19 to 46 ns as follows:

$$R_{i,j}^{\mathrm{norm}}=\frac{NR_{i,j}}{\sum_j R_{i,j}}, \tag{10}$$

where N is the bin number in the TOF region, ranging from 19 to 46 ns. Third, the neutron TOF was converted into neutron energy E_{n} as shown in Fig. 16 and Tables 1 and 2 using [30, 31]:

$$E_{\mathrm{n}}=\left(\frac{1}{\sqrt{1-\frac{L^2}{TOF^2c^2}}}-1\right)m_{\mathrm{n}}c^2, \tag{11}$$

where L is the neutron flight length, c is the speed of light in vacuum, m_{n} denotes the neutron mass. In the present measurement, the influence of relativity can be neglected because the velocity of the detected neutron is much smaller than that of light in vacuum. The calculation of E_{n} can be simplified as [32]:

$$E_{\mathrm{n}}=\frac{5228.16L^2}{TOF^2} \tag{12}$$

where the units of L and TOF are m and ns, respectively.

The measurement uncertainties (1.5% ~ 3.2% at 90°; 1.6% ~ 4.1% at 180°) include those of D and S_{net}. The uncertainties of D (1.5% ~ 3.2% at 90°; 1.6% ~ 4.1% at 180°) comprise statistical uncertainties (1.5% ~ 3.1% at 90°; 1.6% ~ 3.9% at 180°) and the uncertainties from the subtraction of accidental coincidences involving the first neutron (< 0.1% at 90° and 180°), the second neutron (< 0.1% at 90° and 180°) and the γ-ray (< 0.1% at 90° and 180°). The uncertainties of S_{net} (0.2% ~ 0.3% at 90°; 0.2% ~ 0.4% at 180°) consist of statistical uncertainties (0.2% ~ 0.3% at 90°; 0.2% ~ 0.4% at 180°) and uncertainties from the subtraction of accidental coincident backgrounds (< 0.1% at 90° and 180°). The uncertainty of E_{n} (9.5% ~ 17.2%) is contributed by the experimental time resolution of 1.5 ns (6.5% ~ 15.8%) and the uncertainty of the neutron flight path length of 2.15 cm (6.9%).

4.2 Discussions

As shown in Figs. 9 and 16 and Tables 1 and 2, the results indicate that the influence of a neutron on the energy of the correlated neutron is more pronounced in the high energy region, and the related effect at 180° appears to be more noticeable than that at 90°. In addition to the difference in effect magnitude, the correlated neutron energy shows opposite trends between the correlated events at 90° and those at 180°. The energy of the neutron that correlates with a neutron with relatively high energy tends toward a lower value at 90°, while it tends toward a higher value at 180°. With the measured relative ratios, the related neutron energy spectra can be derived by multiplying the relative ratios by the ^{252}Cf prompt fission spectrum recommended by IAEA [23].

When compared with the measurement results obtained by Schuster et al. [14] and the simulation results introduced previously, the present results show the same tendency, i.e., the energy correlation between the coincident neutrons at ~180° is positive, while the energy correlation between the coincident neutrons at ~90° is negative. This further enhances the credibility of the measurement results. In addition, the fact that the measurements and simulations show the same energy correlation tendency indicates that

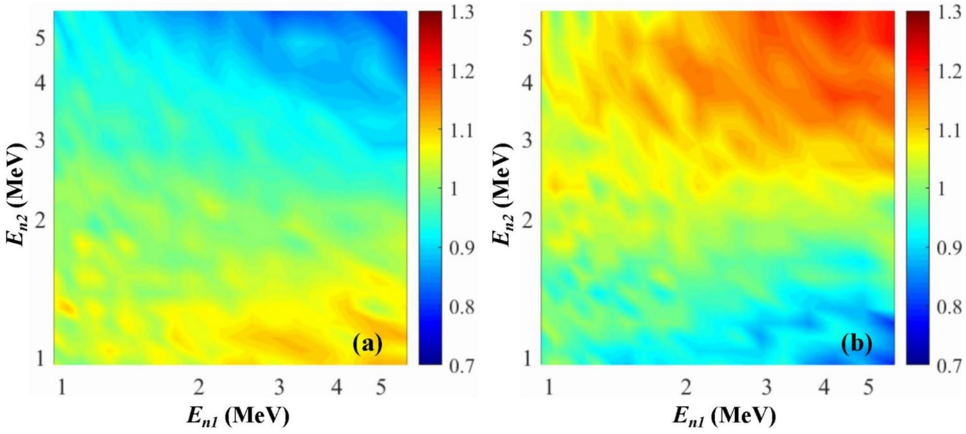

Fig. 16 (Color online) The relative ratios of the measured energy spectra correlated with different energy neutrons at 90° (**a**) and 180° (**b**) to the ^{252}Cf prompt fission neutron energy spectrum

Table 1 The relative ratios of the measured energy spectra correlated with different energy neutrons at 90° to the ^{252}Cf prompt fission neutron energy spectrum

E_{n2} (MeV)	E_{n1} (MeV)									
	0.96±0.09	1.0±0.1	1.1±0.1	1.2±0.1	1.3±0.1	1.4±0.1	1.5±0.2	1.6±0.2	1.8±0.2	1.9±0.2
0.96±0.09	1.01±0.03	1.01±0.03	1.00±0.03	1.03±0.03	1.06±0.03	1.03±0.03	1.04±0.03	1.08±0.03	1.07±0.02	1.04±0.02
1.0±0.1	1.06±0.03	1.06±0.03	1.04±0.03	1.06±0.03	1.10±0.03	1.06±0.03	1.06±0.02	1.09±0.02	1.07±0.02	1.09±0.02
1.1±0.1	1.02±0.03	1.02±0.03	1.01±0.03	1.03±0.03	1.04±0.02	1.03±0.02	1.05±0.02	1.02±0.02	1.08±0.02	1.06±0.02
1.2±0.1	1.01±0.03	1.01±0.03	1.03±0.03	1.05±0.02	1.02±0.02	1.08±0.02	1.07±0.02	1.03±0.02	1.08±0.02	1.06±0.02
1.3±0.1	1.11±0.03	1.11±0.03	1.03±0.02	1.07±0.02	1.03±0.02	1.06±0.02	1.04±0.02	1.06±0.02	1.07±0.02	1.07±0.02
1.4±0.1	1.03±0.02	1.03±0.02	1.03±0.02	1.02±0.02	1.02±0.02	1.04±0.02	1.02±0.02	1.02±0.02	1.03±0.02	1.05±0.02
1.5±0.2	1.00±0.02	1.00±0.02	1.05±0.02	1.06±0.02	1.03±0.02	1.03±0.02	1.04±0.02	1.05±0.02	1.03±0.02	1.04±0.02
1.6±0.2	1.02±0.02	1.02±0.02	1.03±0.02	1.02±0.02	1.05±0.02	1.02±0.02	1.02±0.02	1.01±0.02	1.00±0.02	1.00±0.02
1.8±0.2	1.01±0.02	1.01±0.02	1.08±0.02	1.04±0.02	1.02±0.02	1.06±0.02	1.02±0.02	1.02±0.02	1.01±0.02	1.04±0.02
1.9±0.2	1.01±0.02	1.01±0.02	1.00±0.02	0.96±0.02	1.01±0.02	0.98±0.02	1.01±0.02	1.03±0.02	1.01±0.02	1.02±0.02
2.1±0.3	1.01±0.02	1.01±0.02	1.02±0.02	1.01±0.02	0.99±0.02	1.02±0.02	1.03±0.02	1.03±0.02	0.99±0.02	1.01±0.02
2.3±0.3	1.02±0.02	1.02±0.02	1.00±0.02	1.02±0.02	1.02±0.02	0.99±0.02	0.98±0.02	0.99±0.02	1.00±0.02	1.01±0.02
2.6±0.3	1.01±0.02	1.01±0.02	1.00±0.02	0.99±0.02	1.00±0.02	0.97±0.02	1.01±0.02	0.98±0.02	0.99±0.02	0.96±0.02
2.9±0.4	0.96±0.02	0.96±0.02	0.99±0.02	0.97±0.02	0.95±0.02	0.96±0.02	0.97±0.02	0.95±0.02	0.97±0.02	0.95±0.02
3.3±0.5	0.98±0.02	0.98±0.02	0.95±0.02	0.96±0.02	0.97±0.02	0.96±0.02	0.95±0.02	0.94±0.02	0.98±0.02	0.95±0.02
3.7±0.5	0.96±0.02	0.96±0.02	0.97±0.02	0.93±0.02	0.93±0.02	0.93±0.02	0.94±0.02	0.95±0.02	0.92±0.02	0.93±0.02
4.2±0.6	0.94±0.02	0.94±0.02	0.92±0.02	0.94±0.02	0.94±0.02	0.96±0.02	0.94±0.02	0.93±0.02	0.94±0.02	0.93±0.02
4.9±0.8	0.90±0.02	0.90±0.02	0.92±0.02	0.91±0.02	0.94±0.02	0.89±0.02	0.91±0.02	0.92±0.02	0.90±0.02	0.90±0.02
5.7±1.0	0.96±0.03	0.96±0.03	0.91±0.03	0.92±0.02	0.90±0.02	0.91±0.02	0.90±0.02	0.88±0.02	0.87±0.02	0.87±0.02
	2.1±0.3	2.3±0.3	2.6±0.3	2.9±0.4	3.3±0.5	3.7±0.5	4.2±0.6	4.9±0.8	5.7±1.0	
0.96±0.09	1.08±0.02	1.11±0.02	1.10±0.02	1.08±0.02	1.09±0.02	1.11±0.03	1.10±0.03	1.13±0.03	1.14±0.03	
1.0±0.1	1.07±0.02	1.08±0.02	1.09±0.02	1.11±0.02	1.12±0.02	1.12±0.02	1.09±0.03	1.11±0.03	1.09±0.03	
1.1±0.1	1.06±0.02	1.08±0.02	1.09±0.02	1.10±0.02	1.10±0.02	1.08±0.02	1.05±0.02	1.10±0.03	1.12±0.03	
1.2±0.1	1.08±0.02	1.08±0.02	1.09±0.02	1.08±0.02	1.09±0.02	1.08±0.02	1.10±0.02	1.12±0.03	1.10±0.03	
1.3±0.1	1.08±0.02	1.04±0.02	1.07±0.02	1.08±0.02	1.08±0.02	1.07±0.02	1.11±0.02	1.03±0.02	1.09±0.03	
1.4±0.1	1.04±0.02	1.03±0.02	1.05±0.02	1.07±0.02	1.07±0.02	1.08±0.02	1.10±0.02	1.08±0.02	1.09±0.03	
1.5±0.2	1.02±0.02	1.06±0.02	1.04±0.02	1.06±0.02	1.04±0.02	1.06±0.02	1.06±0.02	1.09±0.02	1.05±0.03	
1.6±0.2	1.02±0.02	1.05±0.02	1.03±0.02	1.06±0.02	1.03±0.02	1.04±0.02	1.07±0.02	1.02±0.02	1.05±0.02	
1.8±0.2	1.03±0.02	1.02±0.02	1.01±0.02	1.02±0.02	0.99±0.02	1.04±0.02	1.03±0.02	1.04±0.02	1.07±0.02	
1.9±0.2	1.01±0.02	1.00±0.02	1.01±0.02	1.02±0.02	1.05±0.02	1.01±0.02	0.99±0.02	1.02±0.02	1.04±0.02	
2.1±0.3	1.06±0.02	1.02±0.02	1.00±0.02	0.98±0.02	1.02±0.02	1.01±0.02	1.01±0.02	1.02±0.02	1.00±0.02	
2.3±0.3	1.00±0.02	0.97±0.02	0.98±0.02	0.98±0.02	0.98±0.02	0.97±0.02	0.96±0.02	0.97±0.02	0.96±0.02	
2.6±0.3	0.98±0.02	0.96±0.01	0.96±0.01	0.97±0.02	0.95±0.02	0.96±0.02	0.95±0.02	0.95±0.02	0.96±0.02	
2.9±0.4	0.96±0.02	0.93±0.01	0.98±0.01	0.94±0.01	0.95±0.02	0.94±0.02	0.96±0.02	0.91±0.02	0.91±0.02	
3.3±0.5	0.93±0.02	0.95±0.02	0.95±0.01	0.94±0.02	0.92±0.02	0.95±0.02	0.91±0.02	0.92±0.02	0.91±0.02	
3.7±0.5	0.94±0.02	0.93±0.02	0.92±0.02	0.93±0.02	0.91±0.02	0.89±0.02	0.89±0.02	0.88±0.02	0.90±0.02	
4.2±0.6	0.91±0.02	0.92±0.02	0.90±0.02	0.88±0.02	0.88±0.02	0.88±0.02	0.89±0.02	0.91±0.02	0.86±0.02	
4.9±0.8	0.89±0.02	0.89±0.02	0.86±0.02	0.88±0.02	0.91±0.02	0.89±0.02	0.88±0.02	0.88±0.02	0.82±0.02	
5.7±1.0	0.85±0.02	0.87±0.02	0.86±0.02	0.82±0.02	0.83±0.02	0.83±0.02	0.85±0.02	0.81±0.02	0.83±0.03	

the dominant reason for this tendency may be the impact of the velocities and directions of fission fragments on the neutron energy. As introduced previously, most neutrons are emitted from fast-moving fission fragments, which means that the moving direction angle between the high-energy neutron and its corresponding fission fragment tends to be small, whereas the moving direction angle between the low-energy neutron and its corresponding fission fragment tends to be large. For the correlated neutrons at 90°, if the energy of the first neutron is relatively high, the energy of the second neutron tends to be low. This is because the relatively high energy of the first neutron indicates a small moving

Table 2 The relative ratios of the measured energy spectra correlated with different energy neutrons at 180° to the ^{252}Cf prompt fission neutron energy spectrum

E_{n2} (MeV)	E_{n1} (MeV)									
	0.96±0.09	1.0±0.1	1.1±0.1	1.2±0.1	1.3±0.1	1.4±0.1	1.5±0.2	1.6±0.2	1.8±0.2	1.9±0.2
0.96±0.09	0.96±0.04	1.01±0.04	0.98±0.04	0.92±0.03	0.97±0.03	0.89±0.03	0.88±0.03	0.92±0.03	0.89±0.03	0.91±0.03
1.0±0.1	0.94±0.04	0.96±0.04	0.95±0.03	0.94±0.03	0.90±0.03	0.91±0.03	0.90±0.03	0.91±0.03	0.91±0.03	0.92±0.02
1.1±0.1	0.91±0.03	0.99±0.03	0.95±0.03	0.93±0.03	0.95±0.03	0.94±0.03	0.94±0.03	0.89±0.02	0.93±0.02	0.88±0.02
1.2±0.1	1.00±0.03	0.97±0.03	0.96±0.03	0.99±0.03	0.97±0.03	0.96±0.03	0.98±0.03	0.95±0.02	0.97±0.02	0.96±0.02
1.3±0.1	0.97±0.03	0.97±0.03	0.99±0.03	0.94±0.03	0.97±0.03	0.95±0.03	0.91±0.02	0.96±0.02	0.96±0.02	0.96±0.02
1.4±0.1	0.99±0.03	0.92±0.03	0.96±0.03	0.97±0.03	0.90±0.02	0.93±0.02	0.99±0.02	0.97±0.02	0.91±0.02	0.95±0.02
1.5±0.2	0.94±0.03	0.95±0.03	0.91±0.03	1.00±0.03	0.97±0.02	0.95±0.02	0.93±0.02	0.95±0.02	1.01±0.02	0.95±0.02
1.6±0.2	0.97±0.03	0.97±0.03	0.98±0.03	0.94±0.02	0.99±0.02	1.00±0.02	0.95±0.02	0.96±0.02	0.96±0.02	0.99±0.02
1.8±0.2	1.00±0.03	1.04±0.03	1.05±0.03	0.98±0.02	1.00±0.02	1.00±0.02	1.02±0.02	1.01±0.02	0.98±0.02	1.02±0.02
1.9±0.2	1.00±0.03	0.99±0.03	1.02±0.03	1.05±0.02	1.00±0.02	1.01±0.02	1.02±0.02	1.03±0.02	1.00±0.02	1.01±0.02
2.1±0.3	1.02±0.03	1.02±0.03	0.99±0.02	1.02±0.02	1.02±0.02	1.04±0.02	0.99±0.02	1.01±0.02	0.98±0.02	1.02±0.02
2.3±0.3	1.03±0.03	1.07±0.03	1.05±0.03	1.06±0.02	0.96±0.02	1.02±0.02	1.05±0.02	1.02±0.02	1.05±0.02	1.00±0.02
2.6±0.3	1.03±0.03	1.05±0.03	1.03±0.02	1.04±0.02	1.05±0.02	1.05±0.02	1.02±0.02	1.03±0.02	1.05±0.02	1.02±0.02
2.9±0.4	1.03±0.03	1.02±0.03	1.01±0.02	1.00±0.02	1.02±0.02	1.04±0.02	1.04±0.02	1.07±0.02	1.04±0.02	1.07±0.02
3.3±0.5	1.03±0.03	1.02±0.03	1.02±0.02	1.06±0.02	1.07±0.02	1.03±0.02	1.05±0.02	1.07±0.02	1.10±0.02	1.05±0.02
3.7±0.5	0.99±0.03	1.06±0.03	1.05±0.03	1.05±0.02	1.07±0.02	1.06±0.02	1.08±0.02	1.10±0.02	1.06±0.02	1.04±0.02
4.2±0.6	1.07±0.03	1.02±0.03	1.01±0.03	1.07±0.03	1.05±0.03	1.08±0.02	1.07±0.02	1.05±0.02	1.07±0.02	1.11±0.02
4.9±0.8	1.05±0.03	1.01±0.03	1.04±0.03	1.04±0.03	1.06±0.03	1.07±0.03	1.10±0.03	1.07±0.02	1.10±0.02	1.10±0.02
5.7±1.0	1.07±0.04	0.98±0.03	1.05±0.03	0.99±0.03	1.07±0.03	1.07±0.03	1.07±0.03	1.02±0.03	1.04±0.03	1.08±0.03

E_{n2} (MeV)	2.1±0.3	2.3±0.3	2.6±0.3	2.9±0.4	3.3±0.5	3.7±0.5	4.2±0.6	4.9±0.8	5.7±1.0
0.96±0.09	0.91±0.02	0.93±0.02	0.90±0.02	0.90±0.02	0.93±0.02	0.86±0.02	0.82±0.02	0.87±0.03	0.78±0.03
1.0±0.1	0.88±0.02	0.89±0.02	0.89±0.02	0.88±0.02	0.91±0.02	0.89±0.02	0.86±0.02	0.85±0.03	0.84±0.03
1.1±0.1	0.89±0.02	0.89±0.02	0.92±0.02	0.84±0.02	0.90±0.02	0.90±0.02	0.90±0.02	0.89±0.03	0.83±0.03
1.2±0.1	0.91±0.02	0.89±0.02	0.88±0.02	0.87±0.02	0.87±0.02	0.84±0.02	0.91±0.02	0.87±0.02	0.78±0.03
1.3±0.1	0.92±0.02	0.93±0.02	0.93±0.02	0.89±0.02	0.91±0.02	0.88±0.02	0.86±0.02	0.87±0.02	0.93±0.03
1.4±0.1	0.94±0.02	0.94±0.02	0.94±0.02	0.97±0.02	0.90±0.02	0.89±0.02	0.91±0.02	0.89±0.02	0.94±0.03
1.5±0.2	0.96±0.02	0.95±0.02	0.97±0.02	0.95±0.02	0.92±0.02	0.97±0.02	0.95±0.02	0.93±0.02	0.97±0.02
1.6±0.2	0.98±0.02	0.94±0.02	0.95±0.02	0.94±0.02	0.94±0.02	0.94±0.02	0.91±0.02	0.89±0.02	0.99±0.02
1.8±0.2	0.99±0.02	0.99±0.02	0.98±0.02	0.99±0.02	0.99±0.02	0.95±0.02	0.95±0.02	0.97±0.02	1.02±0.02
1.9±0.2	0.99±0.02	1.00±0.02	0.97±0.02	0.98±0.02	0.98±0.02	1.00±0.02	0.99±0.02	1.00±0.02	0.99±0.02
2.1±0.3	1.02±0.02	1.02±0.02	1.02±0.02	1.03±0.02	1.01±0.02	1.01±0.02	1.03±0.02	1.02±0.02	0.95±0.02
2.3±0.3	1.05±0.02	1.03±0.02	1.00±0.02	1.02±0.02	1.01±0.02	1.05±0.02	1.01±0.02	1.05±0.02	1.03±0.02
2.6±0.3	1.04±0.02	1.07±0.02	1.05±0.02	1.07±0.02	1.05±0.02	1.06±0.02	1.07±0.02	1.08±0.02	1.11±0.02
2.9±0.4	1.06±0.02	1.05±0.02	1.10±0.02	1.08±0.02	1.10±0.02	1.08±0.02	1.07±0.02	1.10±0.02	1.08±0.02
3.3±0.5	1.09±0.02	1.06±0.02	1.06±0.02	1.10±0.02	1.08±0.02	1.12±0.02	1.11±0.02	1.10±0.02	1.13±0.02
3.7±0.5	1.10±0.02	1.10±0.02	1.10±0.02	1.09±0.02	1.11±0.02	1.12±0.02	1.15±0.02	1.15±0.02	1.14±0.03
4.2±0.6	1.12±0.02	1.10±0.02	1.09±0.02	1.12±0.02	1.10±0.02	1.14±0.02	1.12±0.02	1.13±0.02	1.10±0.03
4.9±0.8	1.06±0.02	1.08±0.02	1.11±0.02	1.13±0.02	1.14±0.02	1.12±0.02	1.16±0.02	1.15±0.03	1.19±0.03
5.7±1.0	1.08±0.02	1.11±0.02	1.12±0.02	1.16±0.02	1.14±0.02	1.18±0.03	1.21±0.03	1.17±0.03	1.20±0.03

direction angle between this neutron and its corresponding fission fragment with a high probability. Therefore, regardless of whether these two neutrons are emitted from the same fission fragment or two different fission fragments, considering the opposite directions of the two fission fragments, the moving direction angle between the second neutron and its corresponding fission fragment is relatively large with a high likelihood. This results in a relatively low energy of the second neutron. Similarly, for correlated neutrons at 180°, a relatively high energy of the first neutron tends to result in low energy of the second neutron if they are emitted from the same fission fragment, but in high energy if they are emitted from different ones. As the probability of detecting neutrons from the same fission fragment is noticeably smaller than that from different fission fragments, the total tendency shows that a high-energy neutron is more likely to be correlated with another high-energy neutron. For example, if each fission fragment emits two neutrons and the detection efficiencies of these neutrons are even, the probability of detecting neutrons from the same fission fragment is approximately half that from different fission fragments. Additionally, it should be noted that the energy correlation should also be contributed by some other factors besides the impact of the velocities and directions of fission fragments, such as the energy competition relationship among the neutrons emitted from the same fission fragment, as pointed out in Ref. [14].

5 Conclusion

The relative ratios of the energy spectra of the neutrons correlated with different energy neutrons to the ^{252}Cf prompt fission spectrum were measured for the first time in the region ranging from 0.96 to 5.7 MeV. The measurement results indicated that the energies of the neutrons emitted from one fission reaction were correlated. The largest deviation between the measured energy spectra of the neutrons correlated with 5.7 MeV neutrons and the fission neutron energy spectra is close to 20%. Furthermore, according to the measured and simulated energy correlation trends, the deviation is expected to be more significant in the higher neutron energy region. This indicates that neutron energy correlations should be considered in the coincidence and multiplication measurement techniques to obtain more reliable measurement results, particularly for fast neutron coincidence and multiplication measurement techniques.

Author Contributions All authors contributed to the study conception and design. Material preparation, data collection and analysis were performed by Huai-Yong Bai, Hang Li, Hong-Jun Zhang, Cheng-Guo Pang, Ming Su, Zhong-Hua Xiong, Ji Wen, Fan Gao, Chen-Guang Li, and Xiao-Dong Wang. The first draft of the manuscript was written by Huai-Yong Bai, Zhong-Hua Xiong and Li-Sheng Yang. All authors commented on the previous versions of the manuscript, read and approved the final version.

Data Availability The data that support the findings of this study are openly available in Science Data Bank at https://cstr.cn/31253.11.sciencedb.j00186.00841 and https://www.doi.org/10.57760/sciencedb.j00186.00841.

Declarations

Conflict of interest The authors declare that they have no conflict of interest.

References

1. M.C. Miller, R.C. Byrd, N. Ensslin et al., Design of a fast neutrons coincidence counter. Appl. Radiat. Isot. **48**(10–12), 1549–1555 (1997). https://doi.org/10.1016/S0969-8043(97)00155-3
2. C. Lee, S. Yoon, S.K. Ahn et al., Fast neutron coincidence counter using scintillators for safeguards verification of the TRU/RE waste. J. Radioanal. Nucl. Chem. **332**(12), 5283–5288 (2023). https://doi.org/10.1007/s10967-023-09084-z
3. M.J. Joyce, K.A.A. Gamage, M.D. Aspinall et al., Real-time, fast neutron coincidence assay of plutonium with a 4-channel multiplexed analyzer and organic scintillators. IEEE Trans. Nucl. Sci. **61**(3), 1340–1348 (2014). https://doi.org/10.1109/TNS.2014.2313574
4. W.X. Xie, J.S. Li, J.Y. Zhu, Uranium mass and neutron multiplication factor estimates from time-correlation coincidence counts. Nucl. Instrum. Methods Phys. Res. A **797**, 182–187 (2015). https://doi.org/10.1016/j.nima.2015.05.066
5. Q.H. Zhang, J.Q. Yang, X.S. Li et al., High order fast neutron multiplicity measurement equations based on liquid scintillation detector. Appl. Radiat. Isot. **152**, 45–51 (2019). https://doi.org/10.1016/j.apradiso.2019.06.022
6. I. Pazsit, N.G. Sjostrand, V. Fhager et al., On the significance of the energy correlations of spallation neutrons on the neutron fluctuations in accelerator-driven subcritical systems. Nucl. Instrum. Methods Phys. Res. A **452**, 256–265 (2000). https://doi.org/10.1016/S0168-9002(00)00350-8
7. Z. Elter, I. Pazsit, Energy correlation of prompt fission neutrons. EPJ Web Conf. **111**, 05003 (2016). https://doi.org/10.1051/epjconf/201611105003
8. W.H. Geist, L.A. Carrillo, L.A. Carrillo et al., Evaluation of a fast neutron coincidence counter for the measurements of uranium samples. Nucl. Instrum. Methods Phys. Res. A **470**, 590–599 (2001). https://doi.org/10.1016/S0168-9002(01)00803-8
9. S.A. Pozzi, S.D. Clarke, W.J. Walsh et al., MCNPX-PoliMi for nuclear nonproliferation applications. Nucl. Instrum. Methods Phys. Res., Sect. A **694**, 119 (2012). https://doi.org/10.1016/j.nima.2012.07.040
10. P. Talou, T. Kawano, I. Stetcu, Prompt fission neutrons and gamma rays in a Monte Carlo Hauser-Feshbach formalism. Phys. Procedia **47**, 39–46 (2013). https://doi.org/10.1016/j.phpro.2013.06.007
11. P. Talou, I. Stetcu, T. Kawano, Modeling the emission of prompt fission γ rays for fundamental physics and applications. Phys. Procedia **59**, 83–88 (2014). https://doi.org/10.1016/j.phpro.2014.10.013
12. J. Randrup, R. Vogt, Calculation of fission observables through event-by-event simulation. Phys. Rev. C **80**(2), 024601 (2009). https://doi.org/10.1103/PhysRevC.80.024601
13. R. Vogt, J. Randrup, Event-by-event study of neutron observables in spontaneous and thermal fission. Phys. Rev. C **84**(4), 044621 (2011). https://doi.org/10.1103/PhysRevC.84.044621
14. P.F. Schuster, M.J. Marcath, S. Marin et al., High resolution measurement of tagged two-neutron energy and angle correlations in ^{252}Cf(sf). Phys. Rev. C **100**, 014605 (2019). https://doi.org/10.1103/PhysRevC.100.014605
15. P. Talou, R. Vogt, J. Randrup et al., Correlated prompt fission data in transport simulations. Eur. Phys. J. A **54**, 9 (2018). https://doi.org/10.1140/epja/i2018-12455-0
16. M.J. Marcath, R.C. Haight, R. Vogt et al., Measured and simulated ^{252}Cf(sf) prompt neutron-photon competition. Phys. Rev. C **97**, 044622 (2018). https://doi.org/10.1103/PhysRevC.97.044622
17. M.X. Kang, J.Z. Zhang, H.Y. Wu et al., Commissioning of the fast neutron detector array at China institute of atomic energy. Nucl. Sci. Tech. **36**, 86 (2025). https://doi.org/10.1007/s41365-025-01649-9

18. T. He, P. Zheng, J. Xiao, Measurement of the prompt neutron spectrum from thermal-neutron-induced fission in U-235 using the recoil proton method. Nucl. Sci. Tech. **30**, 112 (2019). https://doi.org/10.1007/s41365-019-0633-z
19. K. Skarsvag, Time distribution of γ-rays from spontaneous fission of ^{252}Cf. Nucl. Phys. A **153**(1), 82–96 (1970). https://doi.org/10.1016/0375-9474(70)90757-8
20. K. Skarsvag, Time distribution of γ-rays from spontaneous fission of ^{252}Cf at short times. Nucl. Phys. A **253**(2), 274–288 (1975). https://doi.org/10.1016/0375-9474(75)90482-0
21. M. Ellis, C. Tintori, P. Schotanus et al., The effect of detector geometry on EJ-309 pulse shape discrimination performance. In *2013 IEEE Nuclear Science Symposium and Medical Imaging Conference*, Seoul, Korea (South), 2013, pp. 1–6. https://doi.org/10.1109/NSSMIC.2013.6829467
22. C.B. Jorgensen, H.H. Knitter, Simultaneous investigation of fission fragments and neutrons in ^{252}Cf(sf). Nucl. Phys. A **490**, 307–328 (1988). https://doi.org/10.1016/0375-9474(88)90508-8
23. IAEA NEUTRON DATA STANDARDS (2017) https://www-nds.iaea.org/standards/
24. Y.Q. Zhang, L.Q. Hu, G.Q. Zhong et al., Development of a high-speed digital pulse signal acquisition and processing system based on MTCA for liquid scintillator neutron detector on EAST. Nucl. Sci. Tech. **34**, 150 (2023). https://doi.org/10.1007/s41365-023-01318-9
25. Y.Y. Liang, Y.D. Liu, P.S. Wang et al., Optical transmittance and pulse shape discrimination of polystyrene/poly(methyl methacrylate)-based plastic scintillators. Nucl. Sci. Tech. **36**, 9 (2025). https://doi.org/10.1007/s41365-024-01577-0
26. L. Chang, Y. Liu, L. Du et al., Pulse shape discrimination and energy calibration of EJ301 liquid scintillation detector. Nucl. Tech. **38**(2), 1–6 (2015). https://doi.org/10.11889/j.0253-3219.2015.hjs.38.020501. (**in Chinese**)
27. H.Y. Bai, Z.M. Wang, L.Y. Zhang et al., Calibration of an EJ309 liquid scintillator using an AmBe neutron source. Methods Phys. Res. A **863**, 47–54 (2017). https://doi.org/10.1016/j.nima.2017.04.028
28. COMPASS User Manual, CAEN, https://www.caen.it/products/compass/
29. G. Li, B.Y. Zhang, L. Deng et al., Development of Monte Carlo particle transport code JMCT. High Power Laser Part. Beams **25**(1), 158–162 (2013). https://doi.org/10.3788/HPLPB20132501.0158. (**in Chinese**)
30. Q. Li, L.J. Wang, J.Y. Tang et al., ^{10}B-doped MCP detector developed for neutron resonance imaging at Back-n white neutron source. Nucl. Sci. Tech. **35**, 142 (2024). https://doi.org/10.1007/s41365-024-01512-3
31. X.Y. Liu, Y.W. Yang, R. Liu et al., Measurement of the neutron total cross section of carbon at the Back-n white neutron beam of CSNS. Nucl. Sci. Tech. **30**, 139 (2019). https://doi.org/10.1007/s41365-019-0660-9
32. Y.T. Wei, C.L. Lan, B. Gao et al., Benchmark experiment system for ^{252}Cf spontaneous fission source using γ tagging. Nucl. Sci. Tech. **36**, 201 (2025). https://doi.org/10.1007/s41365-025-01776-3